Ultrasonics 141 (2024) 107345

Contents lists available at ScienceDirect

Ultrasonics

journal homepage: www.elsevier.com/locate/ultras

Ultrasonic diffuse bulk wave passive array imaging of internal defects in a complex structure

Zhengjun Wang, Fan Shi *

Department of Mechanical and Aerospace Engineering, Hong Kong University of Science and Technology, Kowloon, Hong Kong Special Administrative Region, China

ARTICLE INFO

Keywords:
Ultrasonic damage detection
Non-destructive evaluation
Diffuse field
Complex structure
Array imaging
Laser vibrometer

ABSTRACT

Ultrasonic bulk wave inspection of defects in safety–critical components with complex external geometries, such as turbine blades is challenging. While ultrasonic phased array imaging can yield high-resolution subsurface images, a commercial phased array probe can hardly be mounted on irregular external boundaries to perform in-situ imaging. In fact, a component with irregular shapes, as a highly reverberant body, is capable of generating elastic random diffuse or coda wavefields. The diffuse wavefields can be utilized to reconstruct Green's functions between any two passive receiving points. In this paper, an ultrasonic passive array imaging method using the diffuse reverberation resulting from complex boundaries is implemented to image internal defects. The method involves the utilization of active piezoelectric actuators to excite elastic diffuse waves within the component, which are received by a laser vibrometer scanning at multiple points. A passive full matrix capture (FMC) of array signals is extracted for defect imaging using the total focusing method. The proposed method is evaluated by the numerical simulations, and the effects of centre frequency, bandwidth, and source excitation methods on the imaging performance are investigated. An experiment using a turbine blade-like structure is conducted to further evaluate the imaging method.

1. Introduction

safety–critical engineering components such as turbine blades, elbows in pipes or complex products made from additive manufacturing often exhibit various complex shapes. The complexity of shape severely limits the use of conventional contact ultrasonic transducers for in-situ inspection of such components, mainly because of the poor coupling with complex boundaries. For example, ultrasonic phased array imaging such as the total focusing method (TFM) [1] has been widely applied because it can produce a high-resolution subsurface image for accurate defect characterization. However, a commercial phased array probe typically has a fixed flat surface and can hardly be mounted on the irregular surface of components. Various acoustic or ultrasonic methods, mainly with non-contact means, have been developed for in-situ inspection of complex components. For example, Farin et al. [2] applied the time-reversal mirror (TRM) technique with a loudspeaker array to remotely detect the damages within the turbine blade, by identifying the shift of natural frequencies of the acoustic signals. Lane et al. [3] applied TFM imaging to detect internal defect, by mounting a phased array at the root of a turbine blade made of single crystalline materials. Water immersed ultrasonic phased array imaging has been developed for imaging the interior defects [4,5], by correcting the ray paths caused by a non-flat surface in the imaging algorithms. Non-contact laser ultrasonic (LU) methods [6,7] provide strong tools to conduct the inspection of specimen with a complex structure. For instance, Wilcox et al. developed a Laser Induced Phased Array (LIPA) method to detect defects [8] and locate features as small as 0.2 mm in diameter in the additive manufactured components [9]. Later, Chen et al. [7] utilized a similar LU imaging methods for detecting internal defects under a curved surface. However, it is also known that the LU technique usually suffers from a relatively lower signal-to-noise ratio (SNR) compared with the piezoelectric transducers, especially if the sample surface is optically non-flat. Besides, LU typically requires a sophisticated system including pulsed laser heads and other optical equipment, with increased hardware complexity and cost. In addition, to improve the signal-to-noise ratio of the signals, higher-energy laser pulses are typically used, which can lead to material damage of the sample, especially for materials with lower melting points. Air-coupled ultrasonic transducers [10,11] have also been applied for inspecting components with irregular boundaries. However, the frequency and the signal amplitude are usually limited.

A component with external boundaries can introduce multiple reflection waves, which interfere with each other, leading to complex waveforms being received. These waves in practice are often considered as strong noise as they may mask the direct defect scattering signal,

* Corresponding author.
E-mail address: maefanshi@ust.hk (F. Shi).

https://doi.org/10.1016/j.ultras.2024.107345
Received 25 February 2024; Received in revised form 9 May 2024; Accepted 12 May 2024
Available online 17 May 2024

imposing difficulties in defect detection. In fact, it is known that ultrasonic wave reverberation in a closed space after a sufficiently long period can result in diffuse/incoherent elastic wavefields [12]. The Green's function between any two measurement points can be extracted in a passive way, by cross-correlating the diffuse signals [13]; this is also known as wave interferometry in seismology [14]. This technique allows to capture the impulse response between two receivers from ultrasonic sources which are remotely excited beyond the area being inspected, leading to more flexible means of collecting defect signals. Extracting the Green's functions for passive imaging was originally developed by the seismic and ocean acoustic communities where the ambient environmental noise usually causes the diffuse field. There have been extensive theoretical and experimental studies [15,16]. The technique was later extended to the ultrasonic community, for instance in the application of NDE [17]. The diffuse state can come from random noise, e.g., temperature fluctuations [18] and structural vibrations [19]. It can also be obtained from actively exciting ultrasonic pulses into the medium in a long period, with one or several actuators [20,21] for applications in structural health monitoring. One of the most popular applications of this technique is post-processing the reconstructed Green's function to conduct the ultrasonic imaging. For instance, Larose et al. [22] demonstrated the experimental method of imaging the surface or buried scatterers from the recovered Green's function. Potter et al. [23] presented the diffused field full matrix capture method to image near surface defects, which can hardly be captured by a conventional phased array. In addition, passive guided wave tomography is developed to realize monitoring of surface defects and corrosion conditions in thin plate structures [20,24,25] without requiring the array system.

For a component with complex shapes, bulk waves reflected back and forth from the boundaries tend to be more random and incoherent; the wavefield is easier to reach the diffuse state in a relatively shorter period, in comparison with a component with regular shapes. Hence, we can take the advantage of the complexity of the boundaries, as they help raise strong diffuse field for passive defect detection. In this paper, we present a diffuse field based ultrasonic array imaging method to detect the internal defects inside a component with a complex shape. We use active sources to generate the diffuse field, and then use a non-contact laser vibrometer to scan the irregular surface of the specimen. The scanning points act as 'virtual' array elements to form a passive full matrix capture (FMC) of the scattered signals, which can be then used for defect imaging.

The paper is organized as follows. In Section 2, the method of retrieving Green's function from random diffuse field and the passive array imaging approach are introduced. In Section 3, two-dimensional finite element (FE) simulations are run to evaluate the accuracy of the passive array imaging method to detect internal defects in a turbine blade-like complex component. The obtained imaging result is compared with those obtained from an active phased array. The imaging performance with different field excitation methods, probing frequencies and bandwidths is also be investigated. In Section 4, an experimental study is conducted to further validate our method using a manufactured turbine blade-like sample. Finally, the conclusions are drawn in Section 5.

2. Methodology

We choose the component with a turbine blade-like shape in all the simulations and experimental studies, for the purpose of method demonstration and the idea can be extended to other complex shapes. The sketch in Fig. 1 describes the overall methodology of passive array imaging, which is briefly introduced here. Active ultrasonic sources such as single element ultrasonic transducers, Lead Zirconate Titanate (PZT) sensors or laser sources can be implemented for exciting the random field. The diffuse field can be generated by exciting sources at spatially random positions while the input signal is a simple narrowband toneburst, which is called the random source location method here. Alternatively, one can also implement a single source at a fixed position, with a broadband random white Gaussian noise (WGN) as the input signal, which is called the broadband excitation method here. The imaging results from the two different excitation methods will be compared in the numerical simulations later. A laser vibrometer is used to scan across the surface of the component to measure displacement signals at multiple points with a fixed interval; these points act as 'virtual' phased array elements to perform imaging. The time cross-correlation is implemented to recover the Green's functions from the recorded diffuse waveforms, yielding a matrix of impulse responses among the measurement points. This is equivalent to performing a full matrix capture (FMC) data collection with a commercial phased array. Finally, the total focusing method (TFM) which is one of the most popular imaging methods in NDE, is implemented to obtain a internal defect image. Note that other array imaging approaches such as diffraction tomography [26] or time reversal [27] can also be applied, based on the matrix of scattering signals measured by a vibrometer. Next, we will review the approach of retrieving the Green's function from the random wavefields. The full matrix capture (FMC) method and the TFM array imaging algorithms considering the irregular surface will also be recalled.

2.1. Retrieve Green's function

As introduced by Weaver et al. [12], the Green's function of an elastic medium can be recovered from the cross-correlation of the diffuse signals in the time domain. The cross-correlation C_T between any two receiving points A and B after a sufficiently long reception time delay t_s can be calculated by:

$$C_T(A,B,t;T) = \frac{1}{T}\int_{t_s}^{t_s+T} S(A,t)S(B,t+\tau)d\tau \tag{1}$$

where $S(A,t)$ and $S(B,t)$ represent the signals recorded at the measuring points A and B, t_s refers to the starting point in the time domain for the cross-correlation, and it needs to be late enough after the wavefield has achieved the diffuse state. The signal amplitude may be attenuated more due to spatial spreading of energy, especially after waves reflected multiple times from the boundaries. So its value needs to be carefully determined to balance against the SNR in the experiment.

T denotes the length of the time window applied to truncate the recorded signals for performing cross-correlation. Ideally the cross-correlation function can be more accurately estimated if the time duration T is sufficiently large. But a very long signal also suffers from amplitude attenuation of its later component as well as noise effects from material scattering. Alternatively, a more feasible solution is to increase the number of random source realizations and perform an average. The statistical cross-correlation C_S can be calculated as:

$$C_S(A,B,t;T) = \lim_{T\to\infty}\sum_{i=1}^{N} C_T(A,B,t;T), \tag{2}$$

where N represents the total number of random source realizations. Averaging over multiple fields effectively reduce the noise level on the reconstructed Green's function. The determination of the values of T and N will be further discussed in the following section. In practice, multiple realizations of source excitations can be achieved by either randomly exciting multiple source positions (i.e., random source location method), or by giving multiple realizations of WGN at a fixed source (i.e., broadband excitation method). If the wave energy is randomly distributed in the space and time domains, it has been proved that [28]:

$$\frac{\partial C_S(A,B,t;T)}{\partial t} \propto G^{+}(A,B,t) - G^{-}(B,A,t), \tag{3}$$

$$S_{P,A,B} = \frac{\partial C_S(A,B,t;T)}{\partial t}, t>0 \tag{4}$$

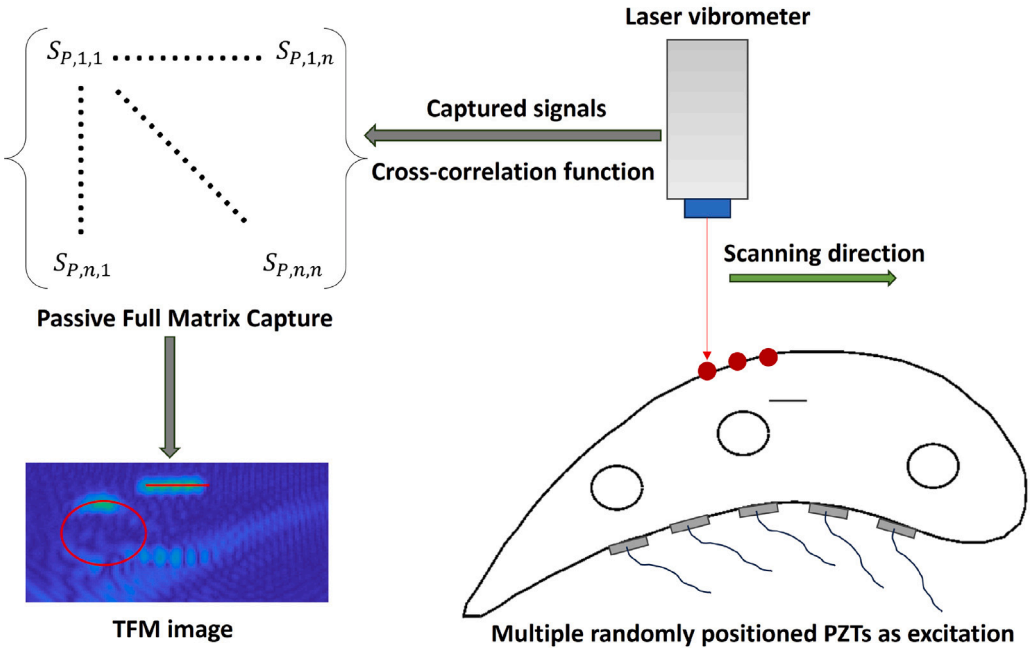

Fig. 1. The sketch of the overall methodology of implementing the diffuse field passive array imaging method to detect the defects and features in a component with an irregular shape.

where G^+ and G^- denote the casual and anti-casual parts of the Green's function, respectively. In this study, the time derivative is numerically approximated by first calculating the finite difference of the signal points, then dividing by the time step. In practice, only the casual part of Green's function $G^+(A, B, t)$ is physically meaningful. Hence, the reconstructed passive signal $S_{P,A,B}$, equivalent to the partial derivative of the statistical cross-correlation function when $t > 0$, is recorded for post-processing.

2.2. Passive full matrix capture and phased array imaging

Once the Green's functions among multiple pairs of measurement points are recovered, a passive full matrix capture (FMC) of signals can be constructed. Specifically, for each measurement point, the passive impulse responses from all the other measurement points are calculated via the cross-correlation operator. For the points which serve as both transmitter and receiver, the auto-correlation function is applied to obtain the Green's function. This procedure is repeated for all the other sensing points. A signal matrix with a dimension of $N_E \times N_E \times N_S$ can be generated, where N_E denotes the total number of 'virtual' array elements and N_S represents the number of signal points in the time domain. By implementing the TFM algorithm, the pixel value I at each imaging position (x', y') can be calculated as [1]:

$$I(x', y') = \frac{1}{N_E^2} \left| \sum_{u}^{N_E} \sum_{v}^{N_E} S_{uv}(t) \right| \tag{5}$$

$$t = \frac{1}{c_p} \left(\sqrt{(x_u - x')^2 + (y_u - y')^2} + \sqrt{(x_v - x')^2 + (y_v - y')^2} \right), \tag{6}$$

where c_p represents the wave speed of the compressional (P) wave, u and v denote the indices of passive array elements for transmitting (virtually) and receiving signal, respectively. (x_u, y_u) and (x_v, y_v) are the coordinates of the transmitting and receiving elements, and (x', y') is the coordinate of the imaging point. $S_{uv}(t)$ refers to the Hilbert transform of time-domain signals.

3. Numerical simulation setup

In this section, high-fidelity FE simulations are run to evaluate the performance of the diffuse field based passive imaging for defect detection in a complex structure. All the simulations are in 2D with the accelerated GPU-based software *Pogo* developed by Huthwaite [29].

3.1. Finite-element modelling

The FE model sketch of a 2D designed cross-section of turbine blade airfoil structure is depicted in Fig. 2. The chord length of a typical blade usually varies from 30 mm to 100 mm [30–32], and here we set the value as 44 mm along the X direction. Within the turbine blade, three circular voids, each with a diameter of 4 mm [33], are introduced to mimic the internal cooling passages. The cooling passages as strong interior scatterers effectively increases the multiple scattering events and aid in the formation of the diffuse state. A horizontally placed smooth crack with a length of 3.6 mm is embedded in the model. In this study, only the P wave is taken into consideration while the method can also be implemented for shear (S) waves. The material is chosen to be Aluminum with a Young's modulus of 70 GPa, Poisson ratio of 0.33, and density of 2700 kg m^{-3}, giving the P wave speed of $c_p = 6198$ m s^{-1}.

Both the random source location method and the broadband excitation method are used in the model. In the first method, a 3-cycle narrow-band toneburst signal is used as the input signal [23]. 50 FE simulations are performed, with the locations of the source nodes distributed randomly at the bottom boundary of model, labelled as yellow stars in Fig. 2. As explained in Eq. (2), by performing an arithmetic averaging of results from multiple source realization, the SNR of the reconstructed Green's function can be significantly improved. Besides, we also investigate the effects of the centre frequencies on the TFM images. Two frequencies 5 MHz and 2.25 MHz, commonly seen in commercial ultrasonic phased arrays are used in the simulations, and the corresponding P wavelengths are 1.24 mm and 2.76 mm, respectively.

In the second method, instead of randomly placing the sources, we fix the source point at one position and use a broadband uncorrelated WGN [34,35] to generate the random diffuse field. Again, 50 realizations of Gaussian noise filtered with two bandwidths of 1–8 MHz and 3–6 MHz are used in the FE simulations. The effects of bandwidth is also evaluated. The total simulation period for both methods is set to be 2 ms, which is long enough to guarantee sufficient multiple

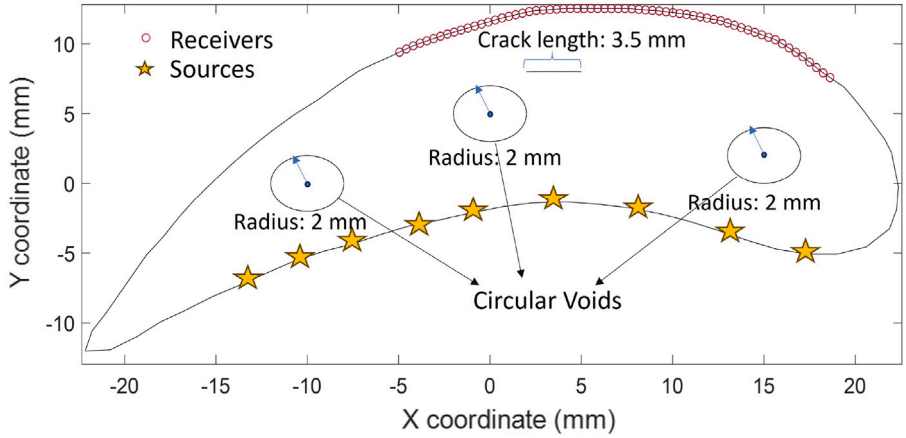

Fig. 2. 2D FE model representing a cross-section of the turbine blade. Three circular voids and a straight crack are included in the model. 64 sensing points (labelled as red circles) are placed on the top surface of the model. The sources are randomly distributed on the bottom boundary of the model, labelled as the yellow stars.

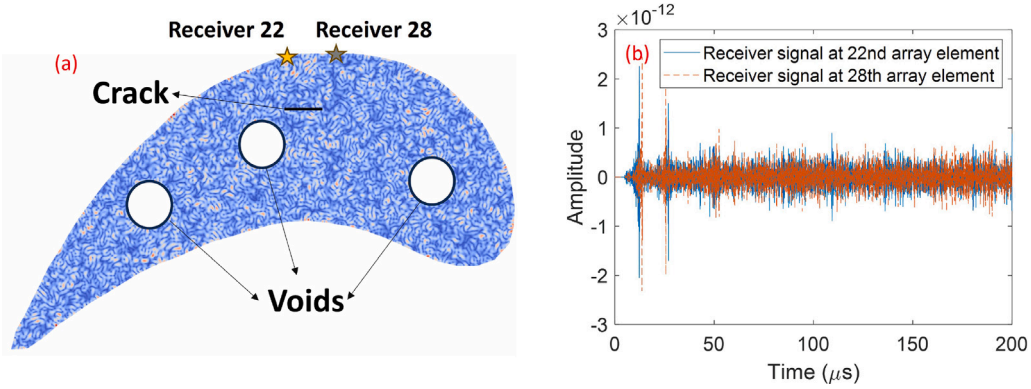

Fig. 3. (a) A snapshot of the diffuse wavefield in the 2D turbine blade model when $t = 150$ μs. (b) The recorded signals at the 22nd (labelled as the blue line) and 28th sensors (labelled as the red dashed line).

reverberations in the component. To receive the diffuse signals, a total of 64 monitoring points (i.e., passive array elements) are placed on the top surface of the turbine blade, as indicated by the red circles in Fig. 2. The horizontal interval of the monitoring points is 0.5 mm, which obeys the spatial sampling law for array imaging. During the FE simulation, only displacements in the Y direction are recorded. An automatic free mesh algorithm is used to mesh the FE model with the plain strain linear triangular element. To ensure convergence, the element size is set as 0.04 mm, which is approximately 1/30 of the P wavelength with a frequency of 5 MHz. The total number of elements in the mesh is around 686,403. Additionally, the computation time step is set to dt $= 2\times10^{-6}$ ms, which is defined by setting the Courant number to be approximately 0.3 [36].

3.2. Green's function extracted from the diffuse waves

In this subsection, the accuracy of retrieving the Green's function from FE simulated diffuse waves is shown. The example results shown here are from the random source location excitation method with 50 different realizations, and the input signal is a 3-cycle toneburst with the centre frequency at 5 MHz. Fig. 3a displays a snapshot of the random wavefield in the FE model at the time step $t = 150$ μs. It has achieved the diffuse state as the wave energy is equally spreaded within the component. The signals captured by the 22nd and 28th sensors with the positions labelled in Fig. 3a, are plotted in Fig. 3b. It can be observed that the diffuse field is formed after around 50 μs.

Eqs. (1), (2), (4) are utilized to retrieve the Green's functions from the diffuse signals. The time window length T is set as 1.8 ms, with the time delay $t_s = 0.2$ ms. The recorded signals from 0.2 ms to 2 ms from the 64 sensors are used to calculate the cross-correlation functions. Note that a longer time window usually provides better reconstruction results but at the expense of higher computation cost. 50 FE simulations from random source excitation are run, and the averaged cross-correlation function is obtained to reconstruct the passive Green's functions. The example of the recovered passive signal between the 22nd and 28th sensors is depicted in Fig. 4. From the waveform, two very strong wavepackets can be identified, emerging at around $t = 1$ μs for the causal Green's function and $t = -1$ μs for the anti-causal Green's function. The strong wave packet corresponds to the creeping waves transmitting directly from the 22nd sensor to the 28th sensor along the boundary. Note that the displayed passive signal exhibits an excellent global symmetry, as expected from the cross-correlation. It serves as an indicator of a high-quality reconstruction. In order to evaluate the accuracy of the recovered Green's function, we run the counterpart FE simulations by setting the 22nd sensor as an excitation point, with the same toneburst signal. The 28th sensor is used to record the scattering signal, denoted as S_{Act}, which is compared with the Green's function obtained from the diffuse field. The passive scattering signal needs to be normalized in the frequency domain to enable the comparison, according to the following equation [24]:

$$\hat{S}^{R}_{P,A,B}(\omega) = \frac{\hat{S}_{Act,A,B}(\omega)}{|\hat{S}_{Act,A,B}(\omega)|}|\hat{S}_{P,A,B}(\omega)|, \tag{7}$$

where $\hat{}$ represents the Fourier transform of the signal, and ω is the angular frequency. Then, the rescaled frequency-domain passive signals are transformed back to the time domain for comparison. Fig. 4b displays the rescaled passive Green's function signal (labelled by a blue line) obtained from cross-correlation, and the active signal (labelled

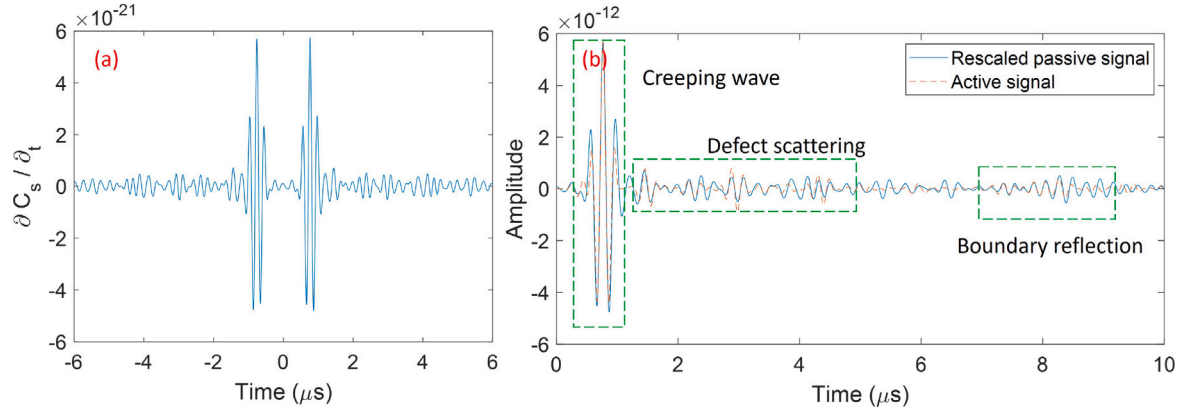

Fig. 4. (a) The recovered passive signal S_P between the 22nd sensor and the 28th sensor. (b) The comparison of rescaled passive and active signals. The rescaled passive signal (blue line) is calculated by Eq. (7). The active signal (red dashed line) is captured by the 28th sensor with the 22nd sensor as the active source. The main wave components such as creeping waves, defect scattering and boundary reflections are highlighted within the green dashed boxes.

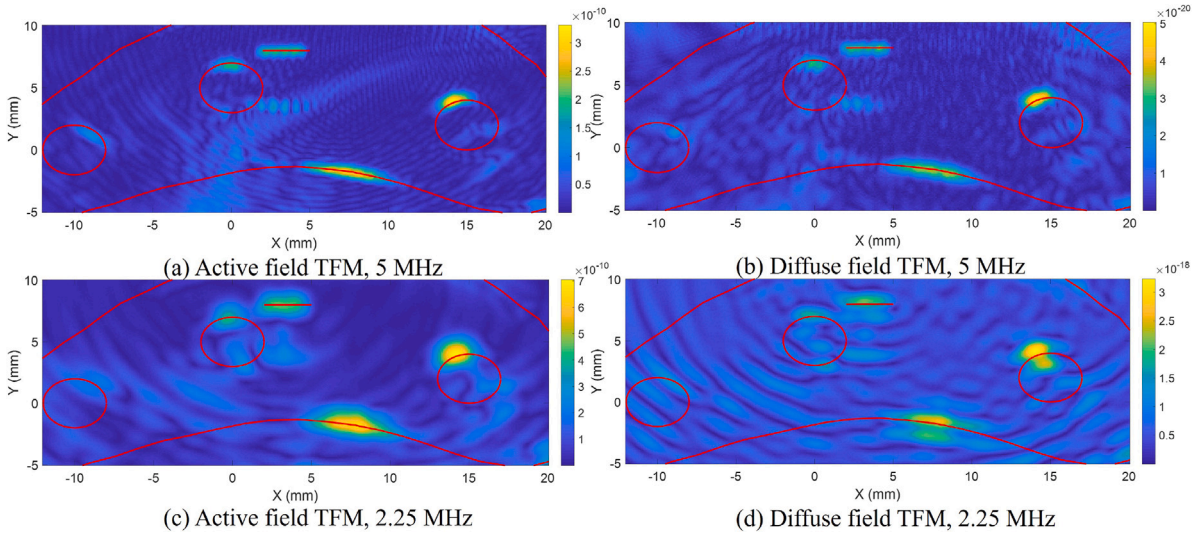

Fig. 5. Comparison of the TFM images obtained using the active field and the passive diffuse field FMC signals with the narrowband toneburst excitation. The red lines represent the boundaries of the turbine blade model including the inner cooling circular channels within the component. (a)(b) The TFM images calculated by the active and diffuse field FMC signals with the centre frequency of 5 MHz, respectively. (c)(d) The TFM images calculated by the active and diffuse field FMC signals with the centre frequency of 2.25 MHz, respectively.

by a dashed red line) directly simulated from the FE model. It can be observed that the main wavepackets (i.e., creeping wave, defect scattering and boundary reflection) of the active and passive signals align well with each other, although some minor disagreement can also be observed. The passive signal contains more noise, and it can be eliminated by increasing the number of random source excitation events. It will be demonstrated in the later subsection that this level of noise has limited impact on the resolution of the TFM images, possibly due to the reason that the incoherent noise is further reduced due to the spatial averaging of TFM. The same method can be used to the broadband WGN excitation method to reconstruct the passive signal matrix for imaging.

3.3. Passive TFM imaging results and discussion

The diffuse field based TFM images can be obtained from Eq. (6), using the recovered passive FMC of signals. The coordinates of array elements are obtained by linear interpolation of the contour curve on the upper surface. Here, we also perform the active wave field TFM imaging with the same array setup and frequency, in order to compare with the passive images obtained from diffuse waves. The conventional FMC involves sequentially emitting Hann-windowed tonebursts with a centre frequency of 5 MHz or 2.25 MHz from the 64 active array elements, and receiving with all the elements. The TFM images obtained from both the active phased array and passive array imaging from the random source location method are compared in Fig. 5. It can be seen that the horizontal crack, the boundary of the turbine blade and most of the cooling passages (e.g., voids) can be clearly identified in all the subplots. The void at the bottom left corner is relatively hard to detect, due to the fact that the array aperture does not cover the scatterer. Besides, the shape of the voids are not well-identified by the TFM images, this is due to the diffraction limit and the limited array aperture size. In Fig. 5b and d, more artifacts appear in the TFM images obtained from the diffuse field in comparison with those from the active phased array. The artifacts are raised by the noise that is not completely averaged out in the recovered Green's function signals as shown in Fig. 5. Besides, when the frequency is reduced from 5 MHz to 2.25 MHz, as shown in Fig. 5c and d, the image resolution becomes relatively lower. However, both active and diffuse field images still yield satisfactory images for identifying defects and boundaries.

In Fig. 6, we plot the TFM images obtained from the diffuse field, when multiple realizations of Gaussian white noise are excited at a fixed source position (i.e., the broadband excitation method). The imaging results depend on the bandwidth of the input noise and here

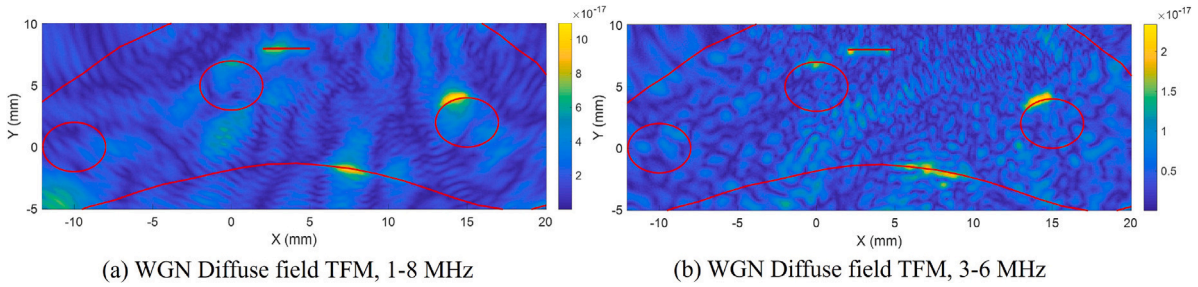

Fig. 6. The TFM images computed using the broadband WGN excitation method. The red lines represent the boundary of the turbine blade model and the cooling channels within the turbine blade. Two bandwidths of input noise are tested. (a) The WGN is filtered within a frequency band of 1 MHz to 8 MHz (b) The WGN is filtered within a frequency band of 3 MHz to 6 MHz.

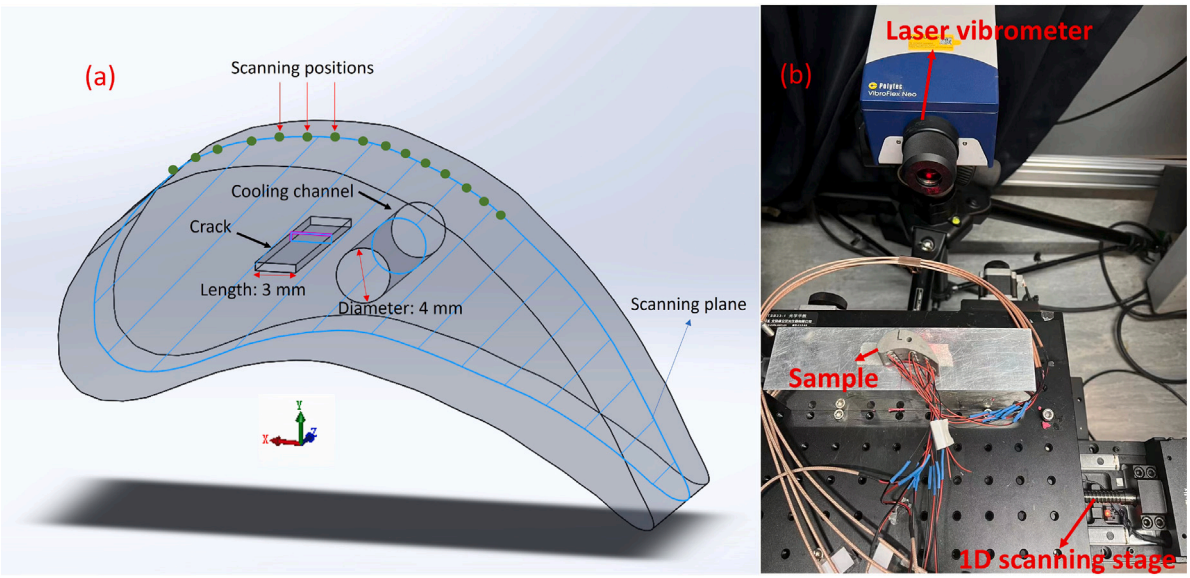

Fig. 7. (a) The sketch of the designed specimen with a 2D turbine blade shape, including a cooling channel and a crack. (b)Photo of the experiment inspection setup. The diffuse wavefields are generated by the PZTs attached on the bottom surface. A laser vibrometer combined with a scanning stage is used to perform the measurement.

we test two different bandwidths (i.e., 1–8 MHz and 3–6 MHz). It can be seen in the figure that although the scatterers and boundary of the turbine blade model are visible, more artifacts can be observed in the TFM image, compared with the narrowband toneburst excitation method. Furthermore, the input signal with a broader bandwidth can yield relatively better TFM image results with a higher SNR.

To summarize the simulation results, the diffuse field TFM imaging can achieve accurate imaging of internal defects in turbine blade-like structures, and the resolution is comparable to active TFM images. Furthermore, the random source location method with narrowband toneburst signals is more suitable for generating random diffuse fields to perform passive TFM imaging. And this will be used in the experimental validation in the next section.

4. Experimental evaluation

In this section, an experiment is conducted to further validate the imaging method using a component with a turbine blade-like shape, manufactured from the computerized numerical control (CNC) machine. The material of the specimen is Aluminum and the 3D sketch of the sample is shown in Fig. 7a. Note that in this study we only consider 2D models, so the sample here has a uniform shape in the z direction. The chord length of blade is 44 mm, consistent with the dimension used in the FE model. The width of the sample along the z-direction is 30 mm. Within the specimen, there is a penetrating cooling channel with a diameter of 4 mm and a horizontal crack with a length of 3 mm.

The experiment setup is depicted in Fig. 7b. To generate the random diffuse field, twelve PZT sensors are glued at random positions on the bottom surface of the specimen. During each source excitation, we excite any two PZTs by applying a Hann-windowed 2.25 MHz, 3-cycle toneburst using the two-channel function generator NI PXIe-5423 (National Instruments Inc., USA). The frequency is chosen considering both the resolution and the amplitude attenuation caused by materials and beam spreading. A power amplifier ATA-1222 A (Aigtek, Xi'an, China) with a gain of 40 dB is used to amplify the signals. A laser vibrometer (Polytech GmbH, Germany) is utilized to remotely measure the vertical (Y direction) surface vibration velocity on the top surface at 24 points, along a line with a spacing of 1 mm. Since the surface vibration velocity is measured by the vibrometer, the time derivative in Eq. (4) is not applied to the experimentally captured signals. The output signals are collected by a digital oscilloscope NI PXI-5105 (National Instruments Inc., USA). We set the total signal recording period as 1 ms, which is sufficiently long to ensure the formation of random wavefields. Additionally, each received signal undergoes 500 times electronic averaging to enhance the SNR. During the measurement, the sample is attached on a three-axis xyz scanning stage, which automatically moves along the x-direction with a step size of 1 mm to conduct the scanning process. To enhance the quality of reconstructed passive signal, 50 realizations of the diffuse fields are generated by exciting different combinations of PZTs.

Fig. 8a shows the recorded raw signals at the 12th and 21st scanning positions. It can be seen that the signals exhibit a high SNR, and the random diffuse field is formed after around 20 μs. To enhance the SNR

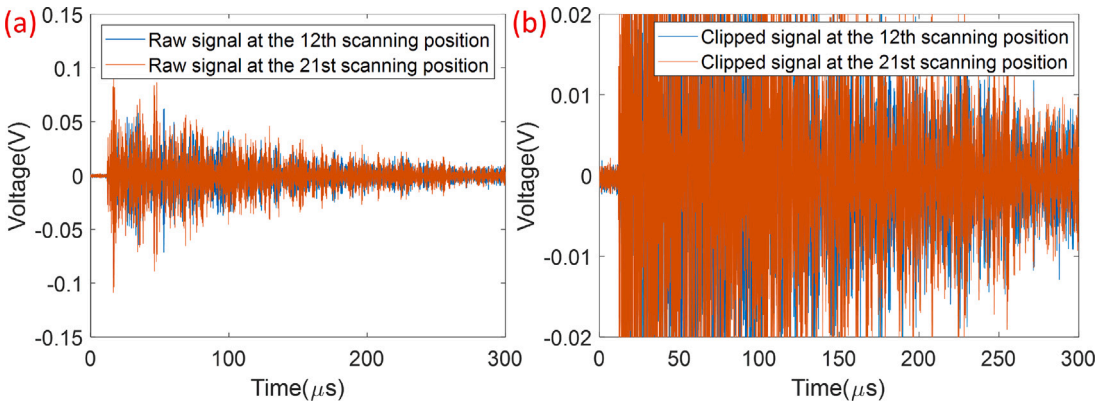

Fig. 8. (a) The raw experimental signals at the 12th and the 21st scanning positions. (b) The clipped raw signals at two positions.

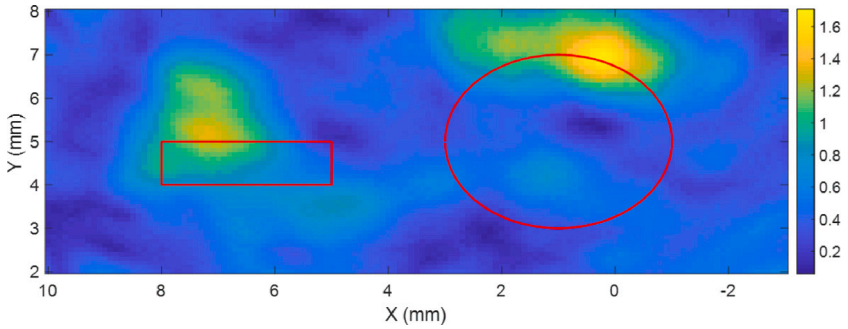

Fig. 9. The passive TFM image obtained from experimental measurements.

of the reconstructed signals, the amplitude of raw signals is clipped to around ten times of the electronic noise level [21], as shown in 8b, before performing cross-correlation. The length of time window T used is 0.8 ms. The reconstructed passive FMC signal matrix is then performed to compute the passive TFM image. Fig. 9 depicts the TFM image of the cooling channel and the crack in the specimen. It can be seen that two distinct scatterers can be identified from the TFM image with a sufficiently high SNR. The crack can be clearly detected, but it is difficult to accurately obtain its features such as size and angle from the image. The discrepancy is primarily attributed to the challenge of achieving ideal reconstruction of passive signals in a real 3D specimen, due to the wave attenuation and material noise. Employing more random source excitation realizations can lead to improved imaging results.

5. Conclusions

In this paper, a passive diffuse field array imaging method is implemented to detect the subsurface defects in an engineering component with a complex shape such as the turbine blade. The diffuse field is excited by random realizations of source locations with a toneburst signal, or by random realizations of Gaussian white noise input at a fixed position. The complexity of shape aids the formation of the diffuse wave field due to the increased multiple reflections from irregular boundaries. The signals received from multiple sensing points are cross-correlated to reconstruct the Green's functions. This allows for forming a virtual passive phased array on a surface with an arbitrary complex shape, via non-contact measurements using a laser vibrometer. A FMC of the scattering signals is obtained and the TFM images are formulated for defect detection and characterization. The method is first evaluated by the high-fidelity FE simulations, and the results show that the passive array imaging can obtain high-resolution images of internal defects and features in a complex structure. The image quality is almost the same as those obtained from the conventional active array imaging method. The performance of different diffuse field excitation methods is compared using the simulated data. The narrowband toneburst excitation method can achieve better imaging results compared with the white Gaussian noise excitation method.

Besides, an experiment is performed with a manufactured turbine blade-like specimen. We use the randomly positioned PZTs to generate the diffuse wavefields in the specimen. A laser vibrometer in conjunction with a 1D scanning stage is used to conduct non-contact reception of diffuse signals, and satisfactory imaging results are obtained. It demonstrates that the passive array imaging method can serve as an alternative solution to the conventional active phased array imaging, particularly when the phased array probe is difficult to be mounted for in-situ inspection of a component with a complex shape.

CRediT authorship contribution statement

Zhengjun Wang: Writing – original draft, Visualization, Validation, Methodology, Investigation. **Fan Shi:** Writing – review & editing, Supervision, Project administration, Funding acquisition, Conceptualization.

Declaration of competing interest

The authors declare that they have no known competing financial interests or personal relationships that could have appeared to influence the work reported in this paper.

Data availability

Data will be made available on request.

Acknowledgements

Z. Wang and F. Shi gratefully acknowledge the support from Foshan HKUST Projects, Hong Kong Special Administrative Region, China [project number: FSUST20-HKUST10E] and Research Grants Council (RGC) of Hong Kong SAR [grant number 26210320].

References

[1] C. Holmes, B.W. Drinkwater, P.D. Wilcox, Post-processing of the full matrix of ultrasonic transmit–receive array data for non-destructive evaluation, NDT E Int. 38 (8) (2005) 701–711, http://dx.doi.org/10.1016/j.ndteint.2005.04.002.

[2] M. Farin, C. Prada, T. Lhommeau, M. El Badaoui, J. de Rosny, Towards a remote inspection of jet engine blades using time reversal, J. Sound Vib. 525 (2022) 116781, http://dx.doi.org/10.1016/j.jsv.2022.116781.

[3] C.J.L. Lane, A.K. Dunhill, B.W. Drinkwater, P.D. Wilcox, The development of a 2D ultrasonic array system for the in situ inspection of single crystal turbine blades, AIP Conf. Proc. 1430 (1) (2012) 865–872, http://dx.doi.org/10.1063/1.4716315.

[4] J. Zhang, B.W. Drinkwater, P.D. Wilcox, Efficient immersion imaging of components with nonplanar surfaces, IEEE Trans. Ultrason. Ferroelectr. Freq. Control 61 (8) (2014) 1284–1295, http://dx.doi.org/10.1109/TUFFC.2014.3035.

[5] R.K. Rachev, P.D. Wilcox, A. Velichko, K.L. McAughey, Plane wave imaging techniques for immersion testing of components with nonplanar surfaces, IEEE Trans. Ultrason. Ferroelectr. Freq. Control 67 (7) (2020) 1303–1316, http://dx.doi.org/10.1109/TUFFC.2020.2969083.

[6] B. Dutton, A. Clough, M. Rosli, R. Edwards, Non-contact ultrasonic detection of angled surface defects, NDT E Int. 44 (4) (2011) 353–360, http://dx.doi.org/10.1016/j.ndteint.2011.02.001.

[7] J. Chen, J. Xiao, D. Lisevych, Z. Fan, Laser-induced full-matrix ultrasonic imaging of complex-shaped objects, IEEE Trans. Ultrason. Ferroelectr. Freq. Control 66 (9) (2019) 1514–1520, http://dx.doi.org/10.1109/TUFFC.2019.2924179.

[8] T. Stratoudaki, M. Clark, P.D. Wilcox, Laser induced ultrasonic phased array using full matrix capture data acquisition and total focusing method, Opt. Express 24 (19) (2016) 21921, http://dx.doi.org/10.1364/OE.24.021921.

[9] D. Pieris, T. Stratoudaki, Y. Javadi, P. Lukacs, S. Catchpole-Smith, P.D. Wilcox, A. Clare, M. Clark, Laser induced phased arrays (LIPA) to detect nested features in additively manufactured components, Mater. Des. 187 (2020) 108412, http://dx.doi.org/10.1016/j.matdes.2019.108412.

[10] E. Blomme, D. Bulcaen, F. Declercq, Air-coupled ultrasonic NDE: Experiments in the frequency range 750kHz–2MHz, NDT E Int. 35 (7) (2002) 417–426, http://dx.doi.org/10.1016/S0963-8695(02)00012-9.

[11] D. Chimenti, Review of air-coupled ultrasonic materials characterization, Ultrasonics 54 (7) (2014) 1804–1816, http://dx.doi.org/10.1016/j.ultras.2014.02.006.

[12] R.L. Weaver, O.I. Lobkis, Diffuse fields in open systems and the emergence of the Green's function (L), J. Acoust. Soc. Am. 116 (5) (2004) 2731–2734, http://dx.doi.org/10.1121/1.1810232.

[13] O.I. Lobkis, R.L. Weaver, On the emergence of the Green's function in the correlations of a diffuse field, J. Acoust. Soc. Am. 110 (6) (2001) 3011–3017, http://dx.doi.org/10.1121/1.1417528.

[14] K. Wapenaar, D. Draganov, R. Snieder, X. Campman, A. Verdel, Tutorial on seismic interferometry: Part 1 — basic principles and applications, GEOPHYSICS 75 (5) (2010) 75A195–75A209, http://dx.doi.org/10.1190/1.3457445.

[15] N.M. Shapiro, M. Campillo, L. Stehly, M.H. Ritzwoller, High-resolution surface-wave tomography from ambient seismic noise, Science 307 (5715) (2005) 1615–1618, http://dx.doi.org/10.1126/science.1108339.

[16] K.G. Sabra, P. Roux, W.A. Kuperman, Emergence rate of the time-domain Green's function from the ambient noise cross-correlation function, J. Acoust. Soc. Am. 118 (6) (2005) 9.

[17] A. Derode, E. Larose, M. Campillo, M. Fink, How to estimate the Green's function of a heterogeneous medium between two passive sensors? application to acoustic waves, Appl. Phys. Lett. 83 (15) (2003) 3054–3056, http://dx.doi.org/10.1063/1.1617373.

[18] R.L. Weaver, O.I. Lobkis, Temperature dependence of diffuse field phase, Ultrasonics 38 (1) (2000) 491–494, http://dx.doi.org/10.1016/S0041-624X(99)00047-5.

[19] K.G. Sabra, E.S. Winkel, D.A. Bourgoyne, B.R. Elbing, S.L. Ceccio, M. Perlin, D.R. Dowling, Using cross correlations of turbulent flow-induced ambient vibrations to estimate the structural impulse response. Application to structural health monitoring, J. Acoust. Soc. Am. 121 (4) (2007) 1987–1995, http://dx.doi.org/10.1121/1.2710463.

[20] L. Chehami, E. Moulin, J. de Rosny, C. Prada, O. Bou Matar, F. Benmeddour, J. Assaad, Detection and localization of a defect in a reverberant plate using acoustic field correlation, J. Appl. Phys. 115 (10) (2014) 104901, http://dx.doi.org/10.1063/1.4867522.

[21] K.G. Sabra, A. Srivastava, F. Lanza di Scalea, I. Bartoli, P. Rizzo, S. Conti, Structural health monitoring by extraction of coherent guided waves from diffuse fields, J. Acoust. Soc. Am. 123 (1) (2008) EL8–EL13, http://dx.doi.org/10.1121/1.2820800.

[22] E. Larose, O.I. Lobkis, R.L. Weaver, Passive correlation imaging of a buried scatterer, J. Acoust. Soc. Am. 119 (6) (2006) 3549–3552, http://dx.doi.org/10.1121/1.2200049.

[23] J. Potter, P. Wilcox, A. Croxford, Diffuse field full matrix capture for near surface ultrasonic imaging, Ultrasonics 82 (2018) 44–48, http://dx.doi.org/10.1016/j.ultras.2017.07.009.

[24] T. Druet, B. Chapuis, M. Jules, G. Laffont, E. Moulin, Passive guided waves measurements using fiber Bragg gratings sensors, J. Acoust. Soc. Am. 144 (3) (2018) 1198–1202, http://dx.doi.org/10.1121/1.5054015.

[25] T. Druet, A. Recoquillay, B. Chapuis, E. Moulin, Passive guided wave tomography for structural health monitoring, J. Acoust. Soc. Am. 146 (4) (2019) 2395–2403, http://dx.doi.org/10.1121/1.5128332.

[26] F. Shi, P. Huthwaite, Ultrasonic wave-speed diffraction tomography with undersampled data using virtual transducers, IEEE Trans. Ultrason. Ferroelectr. Freq. Control 65 (7) (2018) 1226–1238, http://dx.doi.org/10.1109/TUFFC.2018.2828644.

[27] C. Prada, E. Kerbrat, D. Cassereau, M. Fink, Time reversal techniques in ultrasonic nondestructive testing of scattering media, Inverse Problems 18 (6) (2002) 1761–1773, http://dx.doi.org/10.1088/0266-5611/18/6/320.

[28] J. Garnier, G. Papanicolaou, Passive Imaging with Ambient Noise, Cambridge University Press, Cambridge, 2016, http://dx.doi.org/10.1017/CBO9781316471807.

[29] P. Huthwaite, Accelerated finite element elastodynamic simulations using the GPU, J. Comput. Phys. 257 (2014) 687–707, http://dx.doi.org/10.1016/j.jcp.2013.10.017.

[30] O.E. Efe-Ononeme, A. Ikpe, G.O. AriAviE, Modal analysis of conventional gas turbine blade materials (udimet 500 and IN738) for industrial applications, J. Eng. Technol. Appl. Sci. 3 (2) (2018) 119–133, http://dx.doi.org/10.30931/jetas.452857.

[31] I. Pavlenko, S. Kononenko, K. Czernek, S. Witczak, S. Dobrotvorskiy, Y. Basova, V. Ivanov, A. Krupińska, M. Matuszak, S. Włodarczak, M. Ochowiak, An increase in the energy efficiency of axial turbines by ensuring vibration reliability of blade milling, Energies 16 (3) (2023) 1511, http://dx.doi.org/10.3390/en16031511.

[32] B. Li, X. Fan, D. Li, P. Jiang, Design of thermal barrier coatings thickness for gas turbine blade based on finite element analysis, Math. Probl. Eng. 2017 (2017) 1–13, http://dx.doi.org/10.1155/2017/2147830.

[33] S. Feng, A.M. Kamat, Y. Pei, Design and fabrication of conformal cooling channels in molds: Review and progress updates, Int. J. Heat Mass Transfer 171 (2021) 121082, http://dx.doi.org/10.1016/j.ijheatmasstransfer.2021.121082.

[34] F. Jacobsen, T. Roisin, The coherence of reverberant sound fields, J. Acoust. Soc. Am. 108 (1) (2000) 204–210, http://dx.doi.org/10.1121/1.429457.

[35] S. Nakao, T. Hayashi, Non-contact imaging for delamination using diffuse field concept, Japan. J. Appl. Phys. 58 (SG) (2019) SGGB07, http://dx.doi.org/10.7567/1347-4065/ab0ada.

[36] M.B. Drozdz, Efficient Finite Element Modelling of Ultrasound Waves in Elastic Media (Ph.D. thesis), Imperial College London, 2008.